Spectroscopy, Imaging, and Modeling of Individual Gold Decahedra

Jessica Rodríguez-Fernández,*,†,‡ Carolina Novo,‡ Viktor Myroshnychenko,§ Alison M. Funston,‡ Ana Sánchez-Iglesias,† Isabel Pastoriza-Santos,† Jorge Pérez-Juste,† F. Javier García de Abajo,§ Luis M. Liz-Marzán,† and Paul Mulvaney*,‡

Departamento de Química Física and Unidad Asociada CSIC-Universidade de Vigo, 36310 Vigo, Spain, School of Chemistry and Bio21 Institute, University of Melbourne, Parkville, VIC, 3010, Australia, and Instituto de Óptica, CSIC, Serrano 121, 28006 Madrid, Spain

Received: August 7, 2009; Revised Manuscript Received: September 17, 2009

Gold nanodecahedra (pentagonal bipyramids) exhibit striking optical properties spanning the visible and near-IR spectral regions, which together with a high electric-field enhancement at their tips, makes them very promising materials for sensing-related applications. The effective design of biosensors based on these nanocrystals requires a detailed investigation and understanding of their surface plasmon resonances. For that purpose, we have used correlated electron microscopy imaging and optical dark-field spectroscopy on individual decahedra to investigate their size and orientation-dependent optical properties at the single particle level. We have also investigated the effects of tip truncation and local refractive index changes on single particle plasmon resonances. The experimental results are supported by theoretical modeling based on a fully 3D, boundary element method (BEM-3D).

Introduction

Small (nanometer sized) metallic particles exhibit localized surface plasmon resonances due to the collective oscillation of their conduction electrons, induced by external electromagnetic radiation.[1] In the case of gold, localized surface plasmons are usually located in the visible/near-IR spectral window, which opens up a wide range of applications, such as biosensing,[2] photonics,[3] and single molecule detection.[4] For each specific application, a plethora of morphologies (e.g., spheres,[5] rods,[6] prisms,[7] or cubes[8]) and particle sizes within the nanometer range are available as a result of the high degree of shape control achieved over the past decade through colloid chemistry protocols.[9] However, the selection of the most appropriate shape and size for each application demands prior knowledge of the factors determining the optical response of such nanoparticles.

The (localized) surface plasmon resonance of metal nanoparticles is known to be determined by the nature of the metal,[1] the particle size,[10,11] and shape,[12,13] as well as the dielectric properties of the surrounding medium.[13] An increase in particle size (for the same geometry) invariably causes a red shift and broadening of the plasmon bands, due to increased retardation and, eventually, to the appearance of higher order resonances.[14,15] On the other hand, the optical effects derived from the modification of particle morphology are more dramatic, as new plasmon modes become possible. For example, whereas spherical nanoparticles display a single dipole resonance frequency,[5] anisotropic particles, such as rods, can accommodate two dipole modes, as a result of the oscillation of conduction electrons along either of the symmetry axes of the cylinder,[16] and further symmetry breaking generally leads to three distinct dipolar plasmon modes. The same holds for other asymmetric particles, such as nanoplates, where both in-plane and out-of-plane plasmon modes can occur.[7] Since these morphology-derived plasmon resonance modes are independent of one another, they can also be selectively excited by changing the orientation of the anisotropic nanocrystals with respect to the (polarized) incoming light source.[17] This enables exploitation of their angle-dependent optical response.

Solution measurements are invariably influenced by the inhomogeneous broadening effects arising in colloidal ensembles. The optical response is a statistical average over all the various particle shapes, sizes and orientations in the colloidal dispersion. This issue can be overcome by employing techniques that allow the optical characterization of single metallic nanocrystals. Most developments in this area have come from microscopy techniques which permit access to the particles' near-field (e.g., electron energy loss spectroscopy, EELS,[18] and scanning near-field optical microscopy, SNOM[19]) or far-field (total internal reflection microscopy, TIRF,[20] and dark-field microscopy, DFM[21]). Among all these techniques, DFM has experienced increasing attention, mainly due to the simplicity of the instrumental setup. Thus, a large body of work has been devoted to dark-field microspectroscopy characterization, i.e., measurement of the scattering spectra from individual (mainly gold and silver) nanocrystals with various morphologies such as spheres,[22] rods,[21,23] wires,[24] prisms,[25] cubes,[26] or nanostars,[27] among others. Unfortunately, most of these studies to date have not correlated the scattering spectrum (as determined from dark-field microscopy) to the exact size and shape of the investigated nanoparticle.

Decahedral nanocrystals (pentagonal bipyramids) have recently been proposed as sensors for biological applications, due to their optical anisotropy and highly localized plasmon modes.[28,29] In the work described herein, we present a systematic study of the size, specific morphological features, orientation, and local environment dependence of the optical properties of small decahedra at the single particle level, as studied by dark-

* To whom correspondence should be addressed. Fax: +34 986812556. E-mail: jesica@uvigo.es and mulvaney@unimelb.edu.au. Fax: + 61 3 9348 1595.
† Departamento de Química Física and Unidad Asociada CSIC-Universidade de Vigo.
‡ University of Melbourne.
§ Instituto de Óptica.

10.1021/jp907646d CCC: $40.75
Published on Web 10/01/2009

field microspectroscopy in combination with SEM imaging on the very same particle.[30] The discussion below is divided into four sections as follows. In the first part, the single particle and ensemble spectra of gold decahedra are directly compared for a wide range of sizes (40−190 nm, where scattering is intense enough to provide a reasonable signal-to-noise ratio in DFM). Secondly, their angle-dependent optical response is qualitatively investigated. In the third part, the sensitivity of the localized surface plasmon resonance of single particles toward the deposition of a silica shell around the gold cores is demonstrated. In all cases, the experimental data are directly compared to, and supported by, BEM-3D modeling on identical targets.[31−33] Finally, we elucidate the optical effects due to truncation of the lateral tips of the decahedra.

Experimental Section

Chemicals. Tetrachloroauric acid ($HAuCl_4 \cdot 3H_2O$), sodium borohydride ($NaBH_4$), NH_4OH (32%), and tetraethylorthosilicate (TEOS) were purchased from Aldrich. Poly(vinylpyrrolidone) (PVP, M_W 10 000, 40 000 g/mol), 2-propanol, and *N*,*N*-dimethylformamide (DMF) were supplied by Fluka. All chemicals were used as received. Pure grade ethanol and Milli-Q grade water were used to make up all solutions.

Synthesis of Au Decahedra. Gold nanodecahedra (40−190 nm side length) were synthesized according to the protocol developed by Sánchez-Iglesias et al.[28,29] Briefly, a growth solution containing 0.825 mL of aqueous $HAuCl_4$ 0.1136 M in 15 mL of PVP (M_W = 40 000 g/mol) 2.5 mM in DMF was prepared and ultrasonically irradiated until the Au^{3+} charge transfer to solvent (CTTS) absorption band at 325 nm completely disappeared. This was followed by the addition and further sonication of varying volumes of preformed small gold nanoparticle seeds (2−3 nm), to obtain Au bipyramids up to 80 nm side length. Alternatively, larger particles were synthesized by using preformed gold decahedra (43 nm side length) as seeds, while adjusting the $HAuCl_4$ concentration. Truncated decahedra were synthesized with use of 54 nm side length decahedra as seeds (0.4 mL, [Au] = 8 mM) and extracting aliquots at different reaction times. Gold decahedra (50 nm side length) were coated with silica shells (40 nm thick) according to the protocol first reported by Xia and co-workers[34] and modified as described elsewhere.[29]

Sample Preparation for Single Particle Spectroscopy. Indium tin oxide (ITO) coated glass substrates (Delta Technologies, Ltd.) were cleaned (30 min sonication in 2-propanol) and stored in the same solvent for later use. Prior to particle deposition, the slides were dried under an air stream and a poly(methylmethacrylate) (PMMA, M_W = 120 000 g/mol, Aldrich) layer was deposited on the ITO surface by spin-coating (3 s, 5000 rpm) 30 μL of a PMMA solution (1 wt %, in chloroform). The polymer was allowed to dry for at least 2 h at room temperature. Following removal of the excess PVP through several centrifugation/redispersion cycles in ethanol, the decahedra dispersion was conveniently diluted in the same solvent. Then, 30 μL was spin-coated (5 s, 3000 rpm) on the PMMA-covered slide.

Substrate Marking. The as-prepared substrates containing deposited gold nanoparticles were marked by using the focused ion beam (FIB) registration method reported by Novo et al.,[30] as it allows for the easy identification and localization of the gold nanoparticles within a specific area, under both dark-field illumination and scanning electron microscopy (SEM). Box-like patterns (50 μm × 50 μm in size, 1 μm in depth) were milled using the FIB functionality of an xT Nova NanoLab

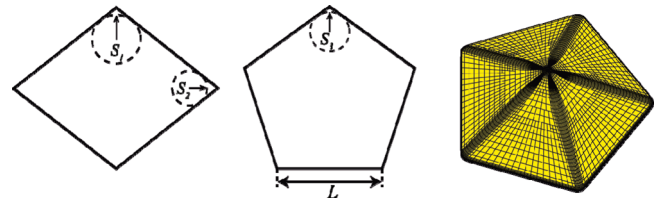

Figure 1. Representative BEM-3D parametrization of a gold decahedron: edge smoothing in sagital and equatorial cross sections (left and center) and final surface tessellation (right).

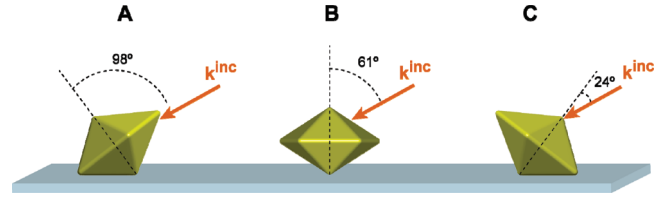

Figure 2. Scheme depicting the three extreme orientations considered for a decahedron on the substrate: lying either on a facet (A, C) or on the bottom apex (B). The unpolarized light impinges on the particle at 61° from the normal to the substrate plane. In all cases, the particles are azimuthally oriented as in part B and the light angle of incidence, measured from the polar axis, is 98° (A), 61° (B), and 24° (C).

SEM. Each box was marked differently in the corners to permit unequivocal identification.

Single Particle Spectroscopy and Imaging. Gold nanoparticles located inside and around the box area were imaged and their scattering spectra acquired using a 100 W halogen lamp illumination source on a Nikon Eclipse TE-2000 inverted optical microscope coupled to a Nikon Dark-field Condenser (Dry, 0.95−0.80 NA). The scattered light from each nanocrystal was collected with a Nikon Plan Fluor ELWD 40×/0.60 NA objective and focused onto the entrance slit of a MicroSpec 2150i imaging spectrometer coupled with a TE-cooled CCD camera (PIXIS 1024B ACTON Princeton Instruments). The light scattered by single decahedra was recorded in the dark-field microscope with collection times ranging from 20 s up to 60 s, as a function of the scattering efficiency of the particles (the larger the particles, the higher the scattering). For direct correlation between particle position and spectra, the box and adjacent areas were imaged and mapped in the DFM. Subsequently, the particles whose spectra were recorded were identified and imaged by SEM (xT Nova NanoLab).

Optical Modeling. The optical responses of the individual gold decahedra were modeled using BEM-3D[33] to calculate the size- and angle-dependent spectra of the particles, as well as the optical changes resulting from silica coating. BEM-3D is based upon rigorous solution of Maxwell's equations, which were recast into surface-integral equations involving auxiliary interface charges and currents.[31,32] It is assumed that the materials involved are described in terms of local, frequency-dependent dielectric functions, taken from tabulated optical data. A typical BEM-3D parametrization of the decahedral particles is schematically shown in Figure 1. For such a morphology, we define the following geometrical parameters: the decahedron side length L, the curvature of the top/bottom apexes of the pyramids S_1, the curvature of the linking edges of the two pyramids S_2, and the curvature of the edges for the azimuthal cross-section of the decahedron S_3. Rounding of the azimuthal tips results in a reduction of the effective decahedron side length (l), which is given by $l = L - 2S_3 \tan(\pi/5)$. Rounding of all edges and tips is not only important to achieve convergence during the calculations, but is also more consistent with the SEM images of the particles. Accordingly, the simulations for a

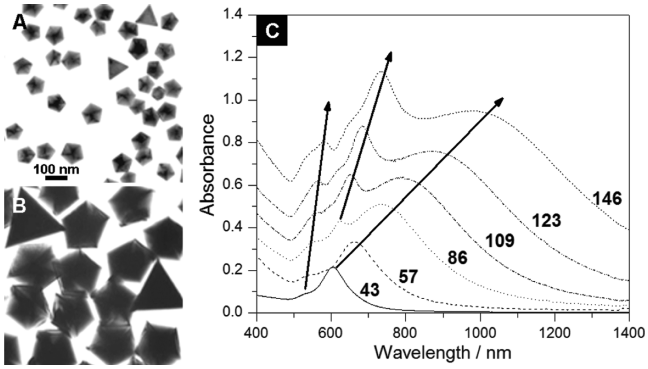

Figure 3. Representative TEM micrographs of gold decahedra grown by using the ultrasound-induced reduction of $HAuCl_4$ in DMF, in the presence of poly(vinylpyrrolidone) (PVP) on preformed 2−3 nm seeds (A) and on preformed gold decahedra (B). The average decahedra edge lengths are 54 (A) and 146 nm (B). The scale is the same for both images. (C) UV−vis−NIR spectra of dispersions of Au decahedra in DMF with varying side lengths (as indicated). The arrows indicate the size dependence of the different plasmonic modes. Adapted with permission from ref 29 (Wiley-VCH, 2007).

decahedron of side length L were carried out considering $L/S_3 = 14.67$, $S_1 = S_3$, and $S_1/S_2 = 1.5$. Edge and tip curvatures can strongly affect the spectral position and width of the plasmon bands.[31,32] Special care has to be given to regions of high curvature. These regions were covered with a denser grid of discretization elements (see Figure 1). The decahedra under investigation were modeled by using ∼5000−8500 boundary elements, depending on the particle size.

Decahedra of different sizes were characterized with the frequency-dependent gold dielectric data measured by Johnson and Christy on gold films.[35] They were considered to be embedded in a homogeneous medium of effective refractive index $n = 1.25$, which approximates the average refractive index experienced by the particles due to the presence of air ($n = 1$) and the PMMA ($n = 1.5$) layer on which the particles are supported. No further consideration of the substrate effect has been made here. To facilitate comparison of the calculated spectra with DFM data and obtain setup-independent results, the simulated elastic scattering cross sections have been averaged over all scattering directions, i.e., they are average cross sections for p- and s-polarized light. Further information on the effect of integration over different collection angles in the calculated elastic cross section of decahedra of various sizes is provided in Figure S1 in the Supporting Information. The particles are assumed to be irradiated with an unpolarized incident plane wave at an angle of 61° relative to the substrate normal. Although each decahedron has a unique orientation relative to the substrate, the simulations of Figure 4C are averages over three extreme orientations, as schematically shown in Figure 2. In the simulations of Figure 6, as well as Figure S1 (Supporting Information), the angle of incidence is varied while keeping the azimuthal orientation as in Figure 2B. Finally, in the simulations of Figure 7, the particle is embedded in a silica sphere ($n = 1.46$) and the spectra are nearly independent of the angle of incidence and the presence of a substrate.

Results and Discussion

1. Single-Particle vs. Ensemble Measurements. The gold decahedra investigated herein were synthesized according to the method developed by Sánchez-Iglesias et al.[28] This protocol allows tight control over the decahedral morphology, together with fine-tuning of particle size and monodispersity. Some representative TEM images of the as-synthesized decahedra are shown in Figure 3A,B, where some triangular prisms obtained as a side product (10−20%) can also be observed.

The size-dependent average optical properties from decahedra ensembles have been extensively studied previously,[28,29] as illustrated in Figure 3C. Typically, the extinction spectra of the smaller particles (ca. 43 nm side) reveal the presence of two distinct dipolar plasmon resonance modes (azimuthal and polar) arising from their anisotropic shape. While the former is associated with oscillations of the conduction electrons along the direction of the pseudo-5-fold symmetry axis, the latter is due to oscillations in the equatorial plane of the particle. The resonance condition for the polar mode is achieved at a higher energy and is also considerably less intense than the azimuthal resonance. As the particle size increases, both modes are red-shifted and broadened and the intensity of the polar resonance becomes slightly more significant. For decahedra larger than ca. 60 nm side length, a new, higher order mode (quadrupolar in nature) starts to develop at an intermediate resonance energy between those of the polar and azimuthal dipoles, gaining intensity as the particles are further enlarged.[29]

We investigated the single particle scattering properties of several individual Au decahedra over a wide size range (40−190 nm). The exact size and morphology of each particle was determined from SEM imaging on the same nanocrystal. Representative examples of such optical/morphological correlation are shown in Figure 4A. In the case of the smaller decahedra (e.g., 54 nm), it is clear that only one plasmon resonance (an azimuthal dipole) is observed in the single particle spectra (black solid line), which is quite different from the ensemble results presented above. Indeed, in none of the measured scattering spectra have we detected the polar plasmon resonance, not even in the largest particles. This may be attributed to the large absorption (and rather low scattering) contribution to the polar mode, which is very likely to overlap with the broadened azimuthal dipole.[29] It is also possible that the orientation of the particles on the substrate precludes excitation of the polar mode, or that excitation does not lead to sufficient light being scattered in the direction of the collection optics. Importantly, the effects of particle size are reflected in the spectra of the individual particles—there is a clear broadening and red shift of the azimuthal resonance, as well as the appearance of a weak shoulder (quadrupole) at higher energy (see below). Nevertheless, direct comparison of the scattering spectra of those individual Au decahedra with the spectra measured from ensembles of particles having the same morphology and (average) size illustrates their significantly narrower line width, since inhomogeneous broadening effects are absent. However, the notable red shift of the ensemble spectra is mainly due to a higher medium refractive index (DMF vs air), as we discuss below.

The results from a statistical single-particle investigation are depicted in Figure 4B. In this graph, the resonance wavelengths of the two plasmon modes, azimuthal dipole (circles) and quadrupole (triangles), are plotted vs. the side length of each individual particle, and each color represents an ensemble of decahedra. Clearly, both modes red shift with increasing particle size and the quadrupole starts to become obvious for particles larger than 90 nm. Particles of the same size exhibit plasmon modes at varying wavelengths, which is more obvious for the larger particles. This effect is also more significant for the dipole mode, providing direct evidence of its higher sensitivity toward changes in either particle morphology or local environment, as demonstrated in earlier single particle[25,36] and ensemble studies[14,37]

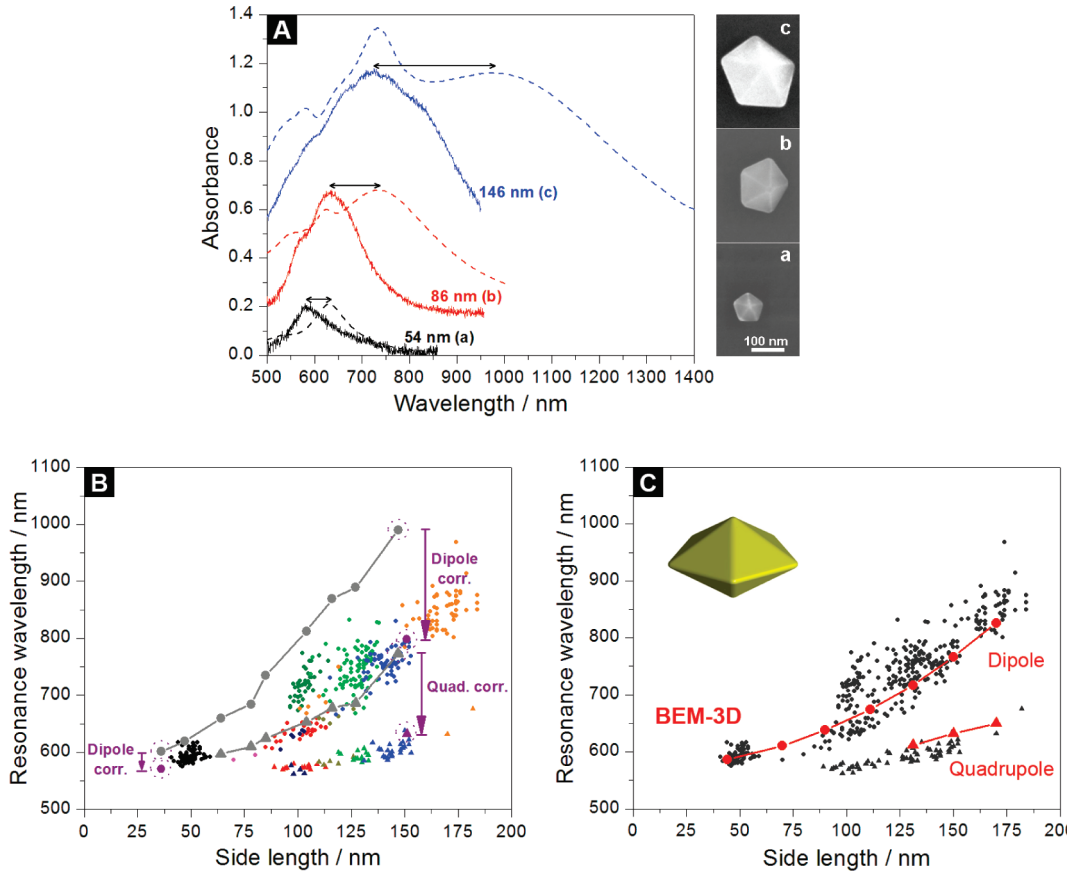

Figure 4. (A, B) Comparison of ensemble and single-particle results. (A) Scattering spectra (full lines) of the Au decahedra shown in the SEM micrographs (side lengths as indicated) and ensemble extinction spectra (in DMF, dashed lines) from colloidal dispersions of particles having the same average side length. Ensemble and single-particle spectra are horizontally offset to improve readability and normalized at their respective azimuthal dipole wavelengths. (B) Evolution of the azimuthal dipole (small colored circles) and quadrupole (small colored triangles) wavelength as a function of the side length of individual decahedra. Each color represents spectra measured from one particular sample. For comparison with the single particle results, the azimuthal dipole (large gray circles) and quadrupole (large gray triangles) resonance wavelengths determined from extinction of decahedra ensembles (DMF as solvent) are also included. The large purple circles and triangles are the refractive-index-corrected data (see text for details). (C) Comparison of the experimental (single particle, gray symbols) vs. calculated (BEM-3D, red symbols) size dependence of the azimuthal dipole (circles) and quadrupole (triangles). A representative BEM-3D parametrization of a decahedron is included as an inset.

for other shapes. In fact, careful examination of the scattering spectrum/SEM micrograph of each decahedron reveals that small morphological differences between particles of the same size can give rise to noticeable plasmon shifts, as we discuss in the Conclusions. Furthermore, as the particles are spin-coated on the substrate, the contact angle of each decahedron relative to the glass support varies from particle to particle. Consequently, maximum plasmon excitation occurs at specific angles of the incident light for each decahedron.

For comparison with the single particle results, the azimuthal dipole and quadrupole wavelengths determined from UV−vis−NIR spectroscopy measurements in decahedra ensembles are included in Figure 4B. Although the trend (red shift) with increasing particle size is the same, it should be noted that the scattering from a single particle is compared to the optical extinction from an ensemble of particles. This holds for all the sizes analyzed, since even for the smallest particles the extinction is dominated by scattering. However, the resonance wavelengths measured in solution, with DMF as solvent ($n = 1.43$), are compared to those of individual decahedra supported on a PMMA-modified ITO-glass slide and exposed to air. Although not completely realistic, this situation can be approximately described by an effective refractive index ($n = 1.25$), equal to the mean of air ($n = 1$) and the substrate/polymer layer ($n = 1.5$).[38] Obviously, the comparison of single particle and ensemble measurements reveals a red-shift of the latter because the refractive index of the solvent is 0.18 units higher. In previous work,[29] the environmental sensitivity of two Au decahedra ensembles (36 and 151 nm average side length) was studied. This allowed us to determine the sensitivity of each plasmon mode to the medium refractive index, and to calculate the expected dipole and quadrupole resonance wavelengths for a medium with $n = 1.25$, equivalent to that of the supported particles (Table 1). Inclusion of the corrected data in Figure 4B (large purple circles/triangles) indicates that the eventual refractive index correction for the remaining sizes would lead to a much better agreement between ensemble and single particle results.

We used three-dimensional parametrization modeling based on the boundary element method (BEM-3D) to calculate the scattering properties of single Au decahedra of various sizes (see details in the Experimental Section). Figure 4C contains the results from these simulations, which agree with the experimental data over the wide range of particle sizes under investigation, thus demonstrating that BEM-3D is a useful computational tool to model the optical response of these highly faceted nanocrystals.[33,39]

2. Orientation Effect. The combination of spectroscopy and imaging on each decahedron makes it possible to directly observe their orientation-dependent optical response. This is illustrated in Figure 5, which shows the scattering spectra of

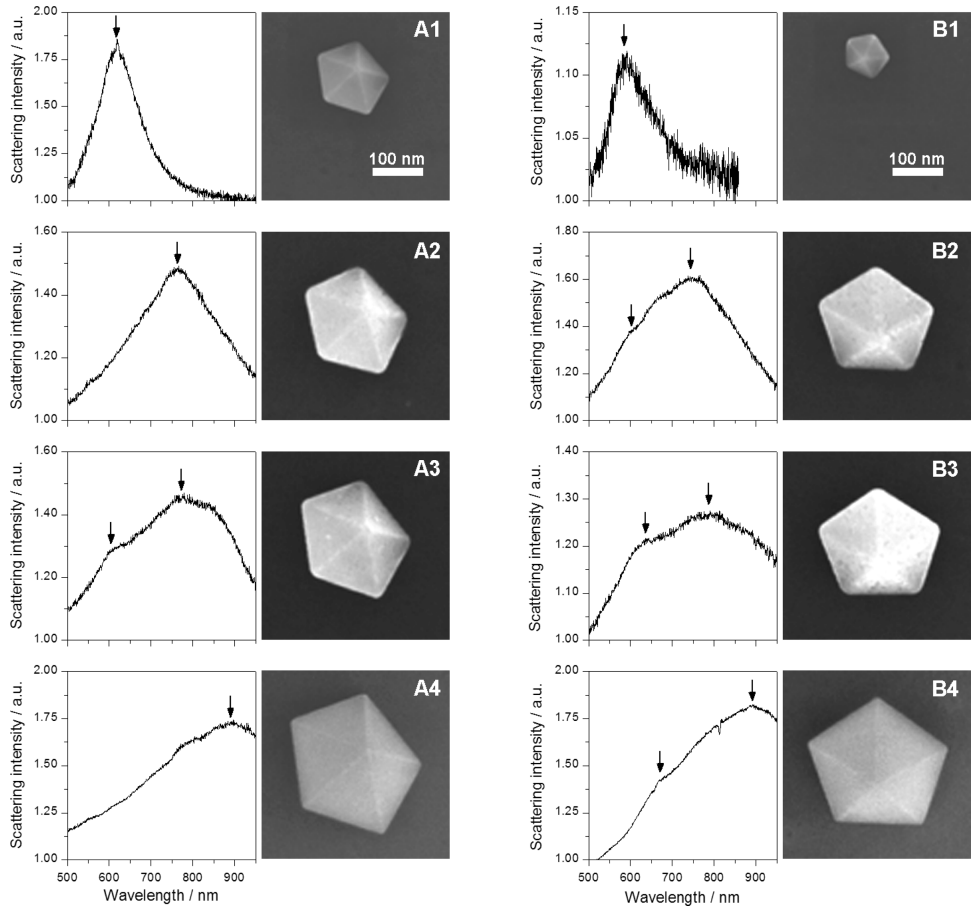

Figure 5. Correlated SEM images/scattering spectra for individual gold decahedra with increasing side length (downward) at two different orientations (A and B) on a PMMA-modified ITO-glass substrate in air. The side length (in nm) and dipole/quadrupole resonance wavelengths (in nm), in brackets, are the following: (A1) 92 (619), (A2) 136 (763), (A3) 148 (774, 614), (A4) 183 (893); (B1) 56 (588), (B2) 141 (752, 597), (B3) 150 (792, 631), (B4) 182 (889, 671). The scale is the same for all SEM images.

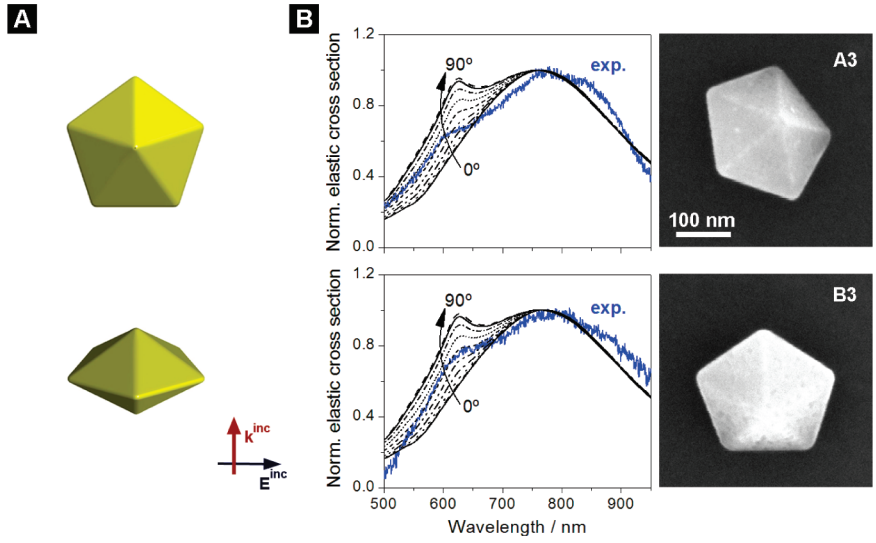

Figure 6. (A) Representative front and side views of the parametrized decahedra. The arrows indicate 0° angle of incidence. (B) Comparison of the experimental spectra of the Au decahedra shown in the SEM images and the calculated elastic cross section for equivalent targets obtained from BEM-3D for different angles of incident light ranging from 0° to 90°, in 10° steps. All the spectra are normalized at the azimuthal dipole maximum. The side lengths of the particles are 148 (A3) and 150 nm (B3).

individual Au decahedra of various sizes for two different orientations with respect to the light source. For both orientations, the increase in particle size results in a red shift of the azimuthal dipole, as well as the appearance of a quadrupolar resonance, as mentioned above. However, the major effect of the particle orientation is on the relative intensities of the quadrupolar and azimuthal dipolar modes. For orientation B in Figure 5 the quadrupole/dipole intensity ratio is systematically higher than in A, indicating that the B orientation is more favorable for the excitation of higher order resonances. It also suggests that the angle-dependent response is more important for the larger decahedra, where higher order modes are more

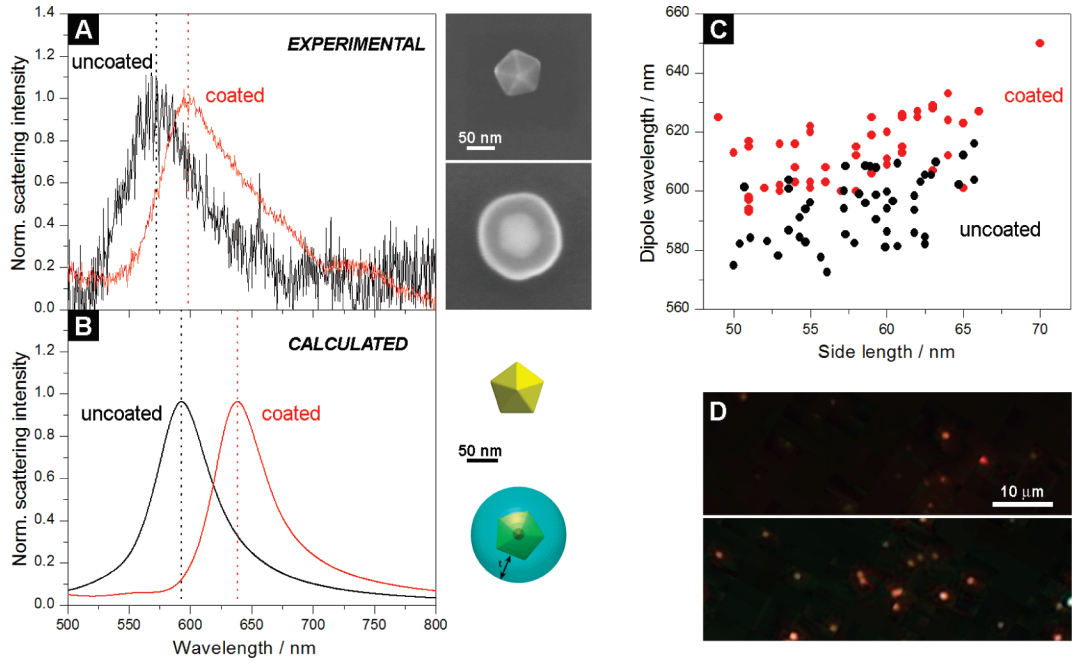

Figure 7. (A) Correlated scattering spectra and SEM images of one bare and one silica-coated (40 nm shell) individual gold decahedron (52 nm side length). (B) Calculated (BEM-3D) scattering spectra for the same particles. The coated decahedron was parametrized as a 52 nm side-length decahedron embedded in a $t = 40$ nm thick silica sphere. (C) Graph illustrating the red shift of the azimuthal dipole of single Au decahedra of various side lengths upon coating with a 40 nm silica shell. (D) Representative DFM images from a batch of uncoated (top) and silica-coated (bottom) Au decahedra.

TABLE 1: Dipole and Quadrupole Environmental Sensitivity (in terms of peak shift per refractive index unit, RIU) As Determined from Optical Extinction Measurements of Two Au Decahedra Dispersions with the Indicated Sizes[a]

⟨side⟩ (nm)	dip. sensitivity (nm/RIU)	quad. sensitivity (nm/RIU)	dip. λ_{max}(nm)	quad. λ_{max}(nm)	dip. λ^*_{max}(nm)	quad. λ^*_{max}(nm)
36	165		601		571	
151	750	307	933	687	798	632

[a] The corresponding resonance wavelengths in DMF are given, as well as the corrected (in 0.18 RIU) values, denoted with asterisks.

TABLE 2: Dimensions (*L*, *l*, and *a*) and Truncation Ratios of the Edge (*L*/*l*) and Top Apices (*a*/*l*) of the Au Decahedra Shown in Figure 9a

particle	*L* (nm)	*l* (nm)	*L*/*l*	*a* (nm)	*a*/*l*	λ_{exp} (nm)
A-a	99	77	1.29	11	0.14	609
A-b	100	62	1.61	17	0.27	599
B-a	94	94	1.00	7	0.07	632
B-b	94	62	1.52	17	0.27	590
C-a	107	107	1.00	8	0.07	641
C-b	107	67	1.60	18	0.27	613

[a] The experimental azimuthal dipole resonances, λ_{exp}, are also given.

likely to occur. This also explains the absence of the quadrupole in the spectrum of particle A1, even though it is large enough (92 nm side length) to exhibit it (see Figure 4B).

Further insight into the optical anisotropy of the decahedra is obtained from modeling. Different orientations of the particles on the substrate are considered in the simulations by varying the angle of incidence of the incoming light. Here, 0° incidence corresponds to the light beam propagating along the direction of the 5-fold axis of the particle, as sketched in Figure 6A. Figure 6B shows the experimental spectra of two decahedra, A3 and B3, selected from Figure 5, compared to the calculated spectra for different angles of incidence. The results confirm the experimental observation that changes in the orientation of the particles produce relatively small shifts in the dipole wavelength, but do strongly influence the relative intensity of the quadrupole: in general, the larger the angle, the higher the quadrupole intensity. In the case of decahedron A3, the particle orientation is better accounted for in the simulation when excitation occurs at an angle of incidence equal to 40°, while for B3 the best agreement is achieved at 50°. This explains the lower quadrupole/dipole intensity ratio in the scattering spectra of the decahedra with orientation A in Figure 5, compared to those with orientation B.

We have calculated the angle-dependent scattering response of Au decahedra of various sizes, and compared them to our experimental data (Figure S2, Supporting Information). Our results show that the angle dependence is more important for the larger particles, as they can accommodate quadrupolar resonances, but it is almost negligible for the smaller ones, at least for the orientations that they exhibit in our experiments. In all cases, the peak wavelengths, intensities, and bandwidths of the modeled spectra are in good agreement with the experimental data collected from single particles.

3. The Effect of Silica Coating. We also examined the optical effects due to the growth of uniform silica shells (40 nm thick) around small, individual gold decahedra of ca. 50−65

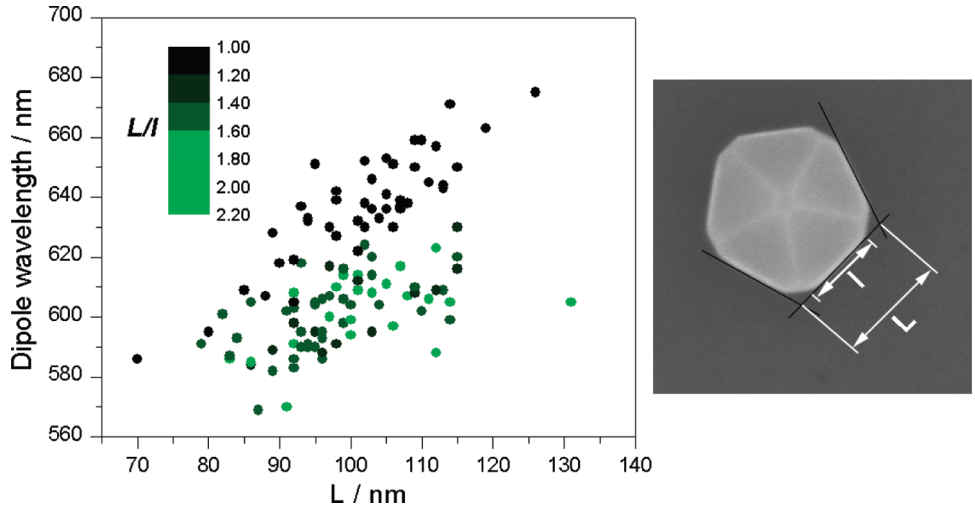

Figure 8. (Left) Effect of truncation on the azimuthal dipolar resonance wavelength, as a function of *L*. (Right): SEM image showing the truncation parameters (*l* and *L*).

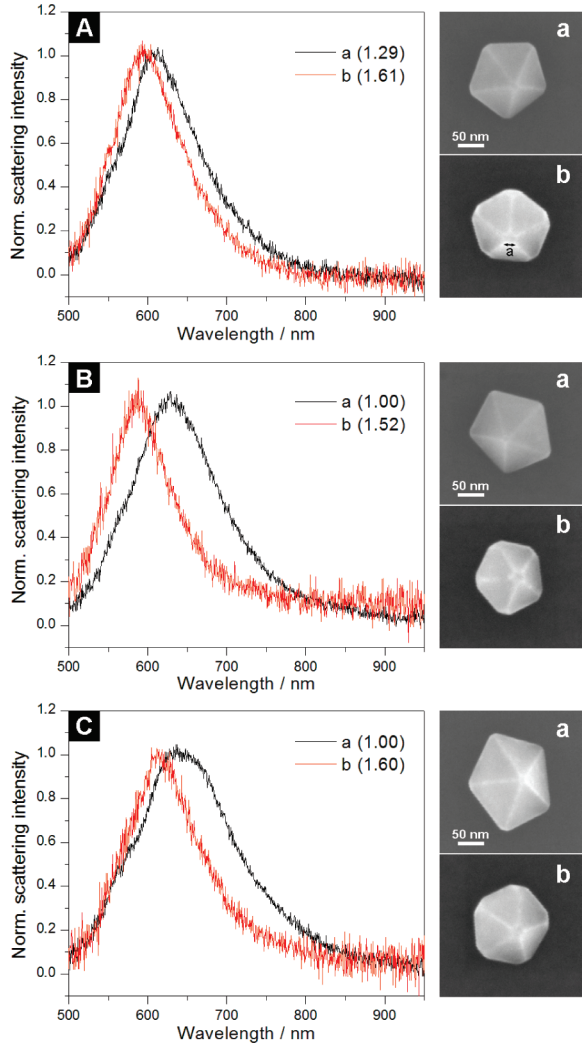

Figure 9. (A−C) Correlated scattering spectra and SEM micrographs of pairs of Au decahedra with increasing tip truncation (indicated in the inset), from (a) to (b), where (a) and (b) have the same effective side length *L*. The truncation parameters and dipole wavelength of the particles are summarized in Table 2. An indication is given in particle A-b of how parameter *a* (tip truncation, see text for details) is measured.

nm side length. The experimental results are illustrated and summarized in Figure 7A,C. The localized azimuthal dipole band undergoes a red shift upon homogeneous coating with amorphous silica, in agreement with ensemble UV−vis−NIR spectroscopy measurements on similar samples.[29] This shift can be unequivocally assigned to the increase in the local refractive index around the particles,[37,40,41] in this case from $n_{eff} = 1.25$ (assuming the particles to be embedded in an average medium of air-glass/PMMA) up to $n = 1.46$ (amorphous silica).[42] Interestingly, the signal-to-noise ratio of the measured scattering spectra (rather low for small, uncoated particles) was significantly improved upon shell growth, which can be attributed to the increase in particle size due to coating. Representative DFM images of the uncoated/coated decahedra samples are shown in Figure 7D.

The effect of silica coating was also modeled by using BEM-3D. The parametrization of a coated particle comprised an Au decahedron embedded in a homogeneous silica sphere. Figure 7B shows the calculated results for the 52 nm decahedron, both uncoated and coated with a $t = 40$ nm thick silica shell, where the thickness *t* is defined in an inset. The simulations reproduce the experimental red-shift upon silica deposition (Figure 7A), even though the plasmon wavelengths do not fully match. These results highlight the extreme sensitivity of individual gold decahedra toward environmental refractive index changes. Consequently, these nanocrystals may have application in optical biosensing.

4. Effect of Truncation. As previously suggested, the morphological features of each decahedron strongly determine its scattering properties. In this section the optical effects derived from truncation of the lateral tips of the decahedra are evaluated. This investigation was carried out via examination of the scattering spectra and SEM images of truncated particles, chosen to be small enough to exhibit a dipole mode in the azimuthal direction only, and therefore with negligible angle-dependent optical response under our experimental conditions. The spectra of these particles are compared with nontruncated ones of the same side length, *L* (see below). The results are summarized in the graph of Figure 8. For each particle, we define the geometrical parameters *l* (the actual side length of a truncated decahedron) and *L* (the side length the decahedron would have if it were not truncated), as shown in the SEM micrograph in Figure 8. Thus, the ratio *L*/*l* is a good indication of the degree of truncation of each nanocrystal: $L/l = 1$ represents a perfect decahedron with sharp tips, whereas a decahedron with truncated edges would have a ratio higher than 1. From the plot, one can

see that a blue shift of the azimuthal dipole occurs with increasing truncation, for the same side length *L*. This blue shift can be justified in terms of the increased number of facets in the truncated decahedron, as compared to the nontruncated one, and may be solely ascribed to truncation, since the difference in the volume of the truncated and nontruncated particles with the same dimension *L* is minimal.

Figure 9 provides some representative examples illustrating the effects of truncation for decahedra pairs with *approximately* the same dimension *L* (data summarized in Table 2). From these data, we can conclude that the extent of the blue shift observed upon truncation depends on the effective particle diameter (in general, the larger the particle, the more sensitive the plasmon band to truncation, as discussed in the Introduction) and the magnitude of *L*/*l*. Another important aspect is the role of the apex truncation, *a* (defined in Figure 9A-b). If *a* is small (this is the most common situation), it is not expected to strongly affect the optical properties, since the charge density induced upon excitation of the azimuthal dipole is mainly localized at the edges, and these are located in the equatorial plane.[29] However, significant apex truncation could induce spectral shifts. Although further theoretical modeling is still needed to gain insight into the relative importance of apex truncation, the observation of a blue shift agrees well with previous DDA calculations on Ag nanoprisms[13,43] and small Ag decahedra.[44]

Conclusions

The optical response of gold nanoparticles with decahedral morphology has been evaluated as a function of the particle size and orientation, via direct correlation of dark-field spectroscopy with SEM images of the same individual nanocrystals. We have shown that a single plasmon resonance (the azimuthal dipole) is observed for the smaller sizes (side lengths 40−90 nm), whereas a quadrupolar mode is discernible for side lengths above 90 nm; both resonance modes red shift with increasing particle size. This trend is in good agreement with previous results obtained from ensemble measurements on colloids of gold decahedra. Additionally, the optical anisotropy of these nanocrystals was qualitatively probed through careful examination of their scattering spectra as a function of orientation toward incoming light. Under our experimental conditions, it was observed that the angle dependence leads to changes in the relative intensity of the quadrupole mode with respect to the dipole resonance, and this effect becomes more important for larger particles. Finally, investigation of the effects derived from coating with silica shells or truncation of the lateral tips of the decahedra has demonstrated the high sensitivity of the particles' localized surface-plasmon modes toward changes in their local environment and to alterations in their morphological features, respectively. The experimental results are further validated through numerical solutions of Maxwell's equations based upon the BEM-3D. Current theoretical models can now accurately predict the optical properties of gold nanocrystals with different morphologies and sizes; however, efforts to understand local refractive index effects are needed for better modeling of surface plasmon based sensors.

Acknowledgment. J.R.-F. acknowledges the Spanish MEC for an FPU scholarship. L.M.L.-M. acknowledges funding from the Spanish MICINN (PCI2005-A7-0075, MAT2007-62696 and Consolider Ingenio NANOBIOMED) and the EU (NANODIRECT, grant no. CP-FP 213948-2). F.J.G.A. acknowledges funding from the Spanish MICINN (MAT2007-66050 and Consolider NanoLight.es) and the EU (NMP4-2006-016881-SPANS and NMP4-SL-2008-213669-ENSEMBLE). P.M. acknowledges funding through the Australian ARC Discovery Projects and Federation Fellow grant schemes via CG 110036 and FF Grant 0561486. A.M.F. acknowledges the support of The University of Melbourne through a Melbourne Research Office Fellowship. The authors thank Sergey Rubanov for assistance with FIB/SEM.

Supporting Information Available: Effect of the scattering collection angles on the calculated (BEM-3D) elastic cross section of 44 and 150 nm decahedra (Figure S1) and calculated (BEM-3D) angle-dependent scattering spectra of 44 and 170 nm Au decahedron (Figure S2). This material is available free of charge via the Internet at http://pubs.acs.org.

References and Notes

(1) Mulvaney, P. *Langmuir* **1996**, *12*, 788–800.
(2) Elghanian, R.; Storhoff, J. J.; Mucic, R. C.; Letsinger, R. L.; Mirkin, C. A. *Science* **1997**, *277*, 1078–1080.
(3) Graf, C.; van Blaaderen, A. *Langmuir* **2002**, *18*, 524–534.
(4) Jiang, J.; Bosnick, K.; Maillard, M.; Brus, L. *J. Phys. Chem. B* **2003**, *107*, 9964–9972.
(5) Turkevich, J.; Stevenson, P. C.; Hillier, J. *Disc. Faraday Soc.* **1951**, *No. 11*, 55–75.
(6) Nikoobakht, B.; El-Sayed, M. A. *Chem. Mater.* **2003**, *15*, 1957–1962.
(7) Pastoriza-Santos, I.; Liz-Marzán, L. M. *Nano Lett.* **2002**, *2*, 903–905.
(8) Sau, T. K.; Murphy, C. J. *J. Am. Chem. Soc.* **2004**, *126*, 8648–8649.
(9) Grzelczak, M.; Perez-Juste, J.; Mulvaney, P.; Liz-Marzan, L. M. *Chem. Soc. Rev.* **2008**, *37*, 1783–1791.
(10) Link, S.; El-Sayed, M. A. *J. Phys. Chem. B* **1999**, *103*, 4212–4217.
(11) Jain, P. K.; Lee, K. S.; El-Sayed, I. H.; El-Sayed, M. A. *J. Phys. Chem. B* **2006**, *110*, 7238–7248.
(12) Link, S.; Mohamed, M. B.; El-Sayed, M. A. *J. Phys. Chem. B* **1999**, *103*, 3073–3077.
(13) Kelly, K. L.; Coronado, E.; Zhao, L. L.; Schatz, G. C. *J. Phys. Chem. B* **2003**, *107*, 668–677.
(14) Kumbhar, A. S.; Kinnan, M. K.; Chumanov, G. *J. Am. Chem. Soc.* **2005**, *127*, 12444–12445.
(15) Rodríguez-Fernández, J.; Pérez-Juste, J.; García de Abajo, F. J.; Liz-Marzán, L. M. *Langmuir* **2006**, *22*, 7007–7010.
(16) Pérez-Juste, J.; Pastoriza-Santos, I.; Liz-Marzán, L. M.; Mulvaney, P. *Coord. Chem. Rev.* **2005**, *249*, 1870–1901.
(17) Pérez-Juste, J.; Rodríguez-González, B.; Mulvaney, P.; Liz-Marzán, L. M. *Adv. Funct. Mater.* **2005**, *15*, 1065–1071.
(18) Nelayah, J.; Kociak, M.; Stephan, O.; García de Abajo, F. J.; Tence, M.; Henrard, L.; Taverna, D.; Pastoriza-Santos, I.; Liz-Marzán, L. M.; Colliex, C. *Nature Phys.* **2007**, *3*, 348–353.
(19) Okamoto, H.; Imura, K. *J. Mater. Chem.* **2006**, *16*, 3920–3928.
(20) Sönnichsen, C.; Geier, S.; Hecker, N. E.; von Plessen, G.; Feldmann, J.; Ditlbacher, H.; Lamprecht, B.; Krenn, J. R.; Aussenegg, F. R.; Chan, V. Z. H.; Spatz, J. P.; Moller, M. *Appl. Phys. Lett.* **2000**, *77*, 2949–2951.
(21) Sönnichsen, C.; Franzl, T.; Wilk, T.; von Plessen, G.; Feldmann, J.; Wilson, O.; Mulvaney, P. *Phys. Rev. Lett.* **2002**, *88*, 077402.
(22) Sönnichsen, C.; Franzl, T.; Wilk, T.; von Plessen, G.; Feldmann, J. *New J. Phys.* **2002**, *4*, 93.
(23) Novo, C.; Gómez, D.; Pérez-Juste, J.; Zhang, Z.; Petrova, H.; Reismann, M.; Mulvaney, P.; Hartland, G. V. *Phys. Chem. Chem. Phys.* **2006**, *8*, 3540–3546.
(24) Mock, J. J.; Oldenburg, S. J.; Smith, D. R.; Schultz, D. A.; Schultz, S. *Nano Lett.* **2002**, *2*, 465–469.
(25) Sherry, L. J.; Jin, R.; Mirkin, C. A.; Schatz, G. C.; VanDuyne, R. P. *Nano Lett.* **2006**, *6*, 2060–2065.
(26) Sherry, L. J.; Chang, S. H.; Schatz, G. C.; Van Duyne, R. P.; Wiley, B. J.; Xia, Y. *Nano Lett.* **2005**, *5*, 2034–2038.
(27) Hao, F.; Nehl, C. L.; Hafner, J. H.; Nordlander, P. *Nano Lett.* **2007**, *7*, 729–732.
(28) Sánchez-Iglesias, A.; Pastoriza-Santos, I.; Pérez-Juste, J.; Rodríguez-González, B.; García de Abajo, F. J.; Liz-Marzán, L. M. *Adv. Mater.* **2006**, *18*, 2529–2534.
(29) Pastoriza-Santos, I.; Sánchez-Iglesias, A.; García de Abajo, F. J.; Liz-Marzán, L. M. *Adv. Funct. Mater.* **2007**, *17*, 1443–1450.
(30) Novo, C.; Funston, A. M.; Pastoriza-Santos, I.; Liz-Marzán, L. M.; Mulvaney, P. *Angew. Chem., Int. Ed.* **2007**, *46*, 3517–3520.
(31) García de Abajo, F. J.; Howie, A. *Phys. Rev. Lett.* **1998**, *80*, 5180.
(32) García de Abajo, F. J.; Howie, A. *Phys. Rev. B* **2002**, *65*, 115418.

(33) Myroshnychenko, V.; Carbó-Argibay, E.; Pastoriza-Santos, I.; Pérez-Juste, J.; Liz-Marzán, L. M.; García de Abajo, F. J. *Adv. Mater.* **2008**, *20*, 4288–4293.

(34) Lu, Y.; Yin, Y.; Li, Z. Y.; Xia, Y. *Nano Lett.* **2002**, *2*, 785–788.

(35) Johnson, P. B.; Christy, R. W. *Phys. Rev. B* **1972**, *6*, 4370–4379.

(36) Rodríguez-Fernández, J.; Funston, A. M.; Pérez-Juste, J.; Álvarez-Puebla, R. A.; Liz-Marzán, L. M.; Mulvaney, P. *Phys. Chem. Chem. Phys.* **2009**, *11*, 5909–5914.

(37) Rodríguez-Fernández, J.; Pastoriza-Santos, I.; Pérez-Juste, J.; García de Abajo, F. J.; Liz-Marzán, L. M. *J. Phys. Chem. C* **2007**, *111*, 13361–13366.

(38) Novo, C.; Funston, A. M.; Pastoriza-Santos, I.; Liz-Marzan, L. M.; Mulvaney, P. *J. Phys. Chem. C* **2008**, *112*, 3–7.

(39) Myroshnychenko, V.; Rodríguez-Fernández, J.; Pastoriza-Santos, I.; Funston, A. M.; Novo, C.; Mulvaney, P.; Liz-Marzán, L. M.; García de Abajo, F. J. *Chem. Soc. Rev.* **2008**, *37*, 1792–1805.

(40) Liz-Marzán, L. M.; Giersig, M.; Mulvaney, P. *Langmuir* **1996**, *12*, 4329–4335.

(41) Pastoriza-Santos, I.; Pérez-Juste, J.; Liz-Marzán, L. M. *Chem. Mater.* **2006**, *18*, 2465–2467.

(42) Palik, E. D., Ed. *Handbook of Optical Constants of Solids*; Academic Press: San Diego, CA, 1985.

(43) Brioude, A.; Pileni, M. P. *J. Phys. Chem. B* **2005**, *109*, 23371–23377.

(44) Noguez, C. *J. Phys. Chem. C* **2007**, *111*, 3806–3819.

JP907646D